

Gamow shell model description of weakly bound nuclei and unbound nuclear statesN. Michel,¹ W. Nazarewicz,^{2,3,4} M. Płoszajczak,¹ and J. Okołowicz⁵¹*GANIL, CEA/DSM-CNRS/IN2P3, BP 5027, F-14076 Caen Cedex 05, France*²*Department of Physics and Astronomy, The University of Tennessee, Knoxville, Tennessee 37996*³*Physics Division, Oak Ridge National Laboratory, P.O. Box 2008, Oak Ridge, Tennessee 37831*⁴*Institute of Theoretical Physics, Warsaw University, ul. Hoża 69, PL-00681, Warsaw, Poland*⁵*Institute of Nuclear Physics, PL-31342 Kraków, Poland*

(Received 20 February 2003; published 22 May 2003)

We present a study of weakly bound, neutron-rich nuclei using the nuclear shell model employing the complex Berggren ensemble representing bound single-particle states, unbound Gamow states, and the non-resonant continuum. In the proposed Gamow shell model, the Hamiltonian consists of a one-body finite depth (Woods-Saxon) potential and a residual two-body interaction. We discuss the basic ingredients of the Gamow shell model. The formalism is illustrated by calculations involving *several* valence neutrons outside the double-magic core: ^{6-10}He and $^{18-22}\text{O}$.

DOI: 10.1103/PhysRevC.67.054311

PACS number(s): 21.60.Cs, 21.10.-k, 24.10.Cn, 24.30.Gd

I. INTRODUCTION

The major theoretical challenge in the microscopic description of weakly bound nuclei is the rigorous treatment of both the many-body correlations and the continuum of positive-energy states and decay channels. A fully symmetric description of the interplay between scattering states, resonances, and bound states in the many-body wave function requires a close interplay between methods of nuclear structure and nuclear reactions. This mutual cross-fertilization, which cannot be accomplished without overcoming a traditional separation between nuclear structure and nuclear reaction methods, is a splendid opportunity for opening a new era in the nuclear theory of loosely bound systems.

In many respects, weakly bound nuclei are much more difficult to treat theoretically than well-bound systems [1]. The major theoretical difficulty and challenge is the treatment of the particle continuum. For weakly bound nuclei (or for nuclear states above the particle threshold), the continuum of positive-energy states and resulting decay channels must be taken into account explicitly. As a result, many cherished approaches of nuclear theory such as the conventional shell model (based on a single-particle basis of bound states) and the pairing theory must be modified.

There are many factors which make the coupling to the particle continuum important. First, even for a bound nucleus, there appears a virtual scattering into the phase space of unbound states. Although this process involves intermediate scattering states, the correlated bound states must be particle stable, i.e., they must have zero width. Second, the properties of unbound states, i.e., above the particle (or cluster) threshold, directly reflect the continuum structure. In addition, continuum coupling directly affects the effective nucleon-nucleon interaction.

The impact of the particle continuum was discussed in the early days of the multiconfigurational shell model (SM) in the middle of the last century. However, thanks to the tremendous success of the large-scale SM in terms of interacting nucleons assumed to be *perfectly isolated* from an *external environment* of scattering states [2–6], the continuum-

related matters had been swept under the rug. An example of an impact of the continuum that goes beyond the standard SM physics is the so-called Thomas-Ehrman shift [7,8] appearing in, e.g., the mirror nuclei ^{13}C and ^{13}N , which is a salient effect of a coupling to the continuum depending on the position of the respective particle emission thresholds. The mathematical formulation of the problem of nuclear states embedded in the continuum of decay channels goes back to Feshbach [9], who introduced the two subspaces containing the discrete and scattering states. Feshbach succeeded in formulating a unified description of nuclear reactions for both direct processes in the short-time scale and compound nucleus processes in the long-time scale. As far as nuclear structure is concerned, the treatment of excited states near or above the decay threshold has been a playground of the continuum shell model (CSM) [10–15]. Unfortunately, a unified description of nuclear structure and nuclear reaction aspects is much more complicated and became possible in realistic situations only at the end of the last century (see Ref. [16] for a recent review).

In the CSM, including the recently developed shell model embedded in the continuum (SMEC) [17–19], the scattering states and bound states are treated on an equal footing. So far, most applications of the CSM, including the SMEC, have been used to describe limiting situations in which there is coupling to *one-nucleon decay channels* only. However, by allowing only one particle to be present in the continuum, it is impossible to apply the CSM to “Borromean systems” for which A and $(A-2)$ nucleon systems are particle-stable but the intermediate $(A-1)$ system is not. Various approaches, including the hyperspherical harmonic method or the coupled-channel approach, have been developed to study structure and reaction aspects of three-body weakly bound nuclei [20–22]. However, most of these models utilize the particle-core coupling which does not allow for the exact treatment of core excitations and the antisymmetrization between the core nucleons and the valence particles.

The reason for limiting oneself to only one particle in the continuum in the CSM has been twofold. First, the number of scattering states needed to properly describe the underly-

ing dynamics can easily go beyond the limit of what present computers can handle. Second, treating the continuum-continuum coupling, which is always present when two or more particles are scattered to unbound levels, is difficult. There have been only a few attempts to treat the multiparticle case [23,24] and, unfortunately, the proposed numerical schemes, due to their complexity, have never been adopted in microscopic calculations involving multiconfiguration mixing. Consequently, an entirely different approach is called for.

Recently, we formulated and tested the multiconfigurational shell model in the complete Berggren basis [25], the so-called Gamow shell model (GSM). (For application to two-particle resonant states, also see Refs. [26,27].) In this paper, the GSM is applied to systems containing several valence neutrons. The single-particle (s.p.) basis of the GSM is given by the Berggren ensemble, which contains Gamow states and the nonresonant continuum. The Gamow states [28] (sometimes called Siegert [29] or resonant states) were introduced for the first time in 1928 to study the α resonances. Gamow defined complex-energy eigenstates $E = E_0 - i\Gamma/2$ in order to describe the particle emission in the quasistationary formalism. Indeed, if one looks at the temporal part of such a state, which is $e^{iE_0 t/\hbar} e^{-\Gamma t/(2\hbar)}$, one notices that the squared modulus of the wave function has the time-dependence $\propto e^{-\Gamma t}$, and one can identify $\hbar/(\Gamma \log 2)$ with the half-life of the system.

Formally, the resonant states are generalized eigenstates of the time-independent Schrödinger equation with purely outgoing boundary conditions. They correspond to the poles of the S matrix in the complex energy plane lying on or below the positive real axis; they are regular in origin and satisfy purely outgoing asymptotics. In the quasistationary approach with Gamow states, each observable O is complex. An interpretation of these complex values has been given by Berggren [30]: the real part of the matrix element gives the average value, while the imaginary part represents the uncertainty of the mean value. This is due to the finite lifetime of the Gamow state which implies that none of the measurements in this state can have a well-defined probability.

In the previous pilot work [25] we showed first applications of the GSM. In this work, we give the details of calculations and demonstrate first applications of the GSM to particle distributions and transition matrix elements.

The paper is organized as follows. Section II discusses how to calculate the matrix elements in the Berggren basis. The completeness relations valid for the single-particle resonant states are briefly reviewed in Sec. III, and some numerical examples involving the Berggren set of the Woods-Saxon potential are presented. Section IV describes the GSM Hamiltonian used in our work. The extension of the completeness relations to the many-body case is described in Sec. V. Sections VI and VII contain the GCM analysis of $^{18-22}\text{O}$ and ^{6-10}He , respectively. Finally, Sec. VIII contains the main conclusions of the paper.

II. MATRIX ELEMENTS IN THE BERGGREN BASIS

Gamow functions are solutions of the Schrödinger equation which are regular at the origin and have the outgoing

wave asymptotics, i.e., the radial part behaves as e^{ikr} at large distances. In the case of the spherical one-body potential, the resonant wave function $\phi_{nj\ell}$ carrying the s.p. angular momentum ℓ_j can be written as a product of the usual angular part and the radial wave function $u_{nj\ell}(r)/r$. It is customary to introduce the notation

$$\bar{u}_{nj\ell}(r) = u_{nj\ell}(r)^*, \quad (1)$$

$$\bar{\phi}_{nj\ell} = \phi_{nj\ell}(u \rightarrow \bar{u}). \quad (2)$$

For bound states, one can always introduce a phase convention which makes the radial wave function real. That is, for bound states $\bar{\phi}_{nj\ell} = \phi_{nj\ell}$. The following discussion concerns the specific properties of the radial Gamow wave functions $u_{nj\ell}(r)$. Of course, one should always remember that the angular part is always present, but its treatment is standard. Consequently, in the GSM, only radial matrix elements require special attention.

A. Normalization of Gamow states and one-body matrix elements

The norm N_i of a resonant state,

$$N_i^2 = \int_0^{+\infty} u_i^2(r) dr, \quad (3)$$

and the radial matrix elements calculated in the Berggren basis,

$$O_{if} = \int_0^{+\infty} u_f(r) O(r) u_i(r) dr, \quad (4)$$

are diverging, but this difficulty can be avoided by means of a regularization procedure [31–36]. Zel'dovich proposed multiplying the integrand of a radial matrix element by a Gaussian convergence factor [31]:

$$\begin{aligned} \langle u_f | O | u_i \rangle &= \lim_{\epsilon \rightarrow 0} \int_0^{+\infty} e^{-\epsilon r^2} u_f(r) O(r) u_i(r) dr \\ &= \text{Reg} O_{if}. \end{aligned} \quad (5)$$

In this expression, $|u_f\rangle$ and $|u_i\rangle$ stand for single-particle states, $O(r)$ is a radial part of a one-body operator, and $\text{Reg} O_{ij}$ stands for the regularized matrix element O_{ij} . Using the Zel'dovich regularization method, Berggren has shown [34] that the Gamow states, together with scattering states, form a complete basis. In particular, using definition (5) with $O(r) = 1$, one can demonstrate that all Gamow states can be orthonormalized, and such orthonormalized functions can be used to calculate matrix elements. Unfortunately, the method of Zel'dovich, even though important on formal grounds, cannot be used in numerical applications due to the difficulty in approaching the limit in Eq. (5) for diverging integrals.

An equivalent and more practical procedure, justified by the apparatus of the analytical continuation, was proposed by Gyarmati and Vertse [35]. For that, let us define the following functional on $(-\infty; V_{\text{lim}}]$ [37]:

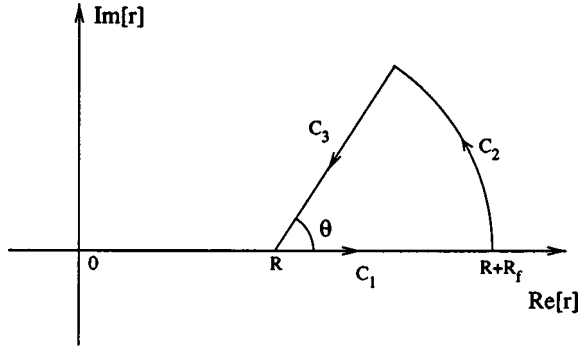


FIG. 1. The path in the complex coordinate space corresponding to the complex rotation by angle θ . R is the point from which the exterior complex rotation starts. R is large as compared to the nuclear radius; hence it is assumed that the nuclear potential is negligible for $r > R$.

$$F(V_o) = \frac{O_{ij}}{N_i N_f}, \quad (6)$$

where V_o is the depth of the potential generating s.p. wave functions u_f and u_i , V_{lim} is the depth of the potential for which one of these functions is bound and the other one is at zero energy, and $O(r)$ is some analytical operator. This functional is defined in such a way because the integral converges in the domain $(-\infty; V_{\text{lim}})$. It represents the radial matrix element $\langle u_f | O | u_i \rangle / \|u_f\| \|u_i\|$ between two not necessarily normalized wave functions. Since u_f and u_i are bound, one can make them real, $u_f^* = u_f$, $u_i^* = u_i$. In Ref. [37], the analytical continuation of F is made using the Padé approximants. In the present work we shall refer to the technique of the complex rotation [35] which allows a calculation of F with $V_o > V_{\text{lim}}$. To see that, let us call $f(r)$ one of three integrands $u_f(r)O(r)u_i(r)$, $u_f^2(r)$, or $u_i^2(r)$ and let us take $V_o < V_{\text{lim}}$. Since f is analytical on \mathbb{C} (see Fig. 1), then, following the Cauchy theorem, one has

$$\int_{C_1} f(z) dz + \int_{C_2} f(z) dz + \int_{C_3} f(z) dz = 0. \quad (7)$$

Since f decreases exponentially for $\text{Re}[z] > 0$, the integral $\int_{C_2} f(z) dz \rightarrow 0$ if $R_f \rightarrow +\infty$. For the same reason, the integrals $\int_{C_1} f(z) dz$ and $\int_{C_3} f(z) dz$ converge if $R_f \rightarrow +\infty$. Consequently, for $R_f \rightarrow +\infty$ one obtains

$$\int_R^{+\infty} f(r) dr = \int_0^{+\infty} f(R+x \cdot e^{i\theta}) e^{i\theta} dx. \quad (8)$$

Hence, on the interval $(-\infty; V_{\text{lim}})$, one can define F by Eq. (6), with norm (3) given by

$$N_i = \sqrt{\int_0^R u_i^2(r) dr + \int_0^{+\infty} u_i^2(R+x \cdot e^{i\theta}) e^{i\theta} dx}, \quad (9)$$

and with the matrix element (4) of the form

$$O_{if} = \int_0^R u_f(r) O(r) u_i(r) dr + \int_0^{+\infty} [u_f(R+x \cdot e^{i\theta}) \times O(R+x \cdot e^{i\theta}) \times u_i(R+x \cdot e^{i\theta}) e^{i\theta} dx]. \quad (10)$$

If u_f and u_i are bound- or decaying-state wave functions, one can write $k_f = |k_f| e^{-i\alpha_f}$ and $k_i = |k_i| e^{-i\alpha_i}$. As $u_f(z) \sim a_f(z) e^{ik_f z}$ and $u_i \sim a_i(z) e^{ik_i z}$ when $\text{Re}[z] \rightarrow +\infty$, with a_f and a_i the algebraic increasing functions, the integrals defining F converge if one takes

$$\theta > \alpha_f + \alpha_i. \quad (11)$$

In addition, the expression for F is analytical because F is a function of converging integrals of analytical functions. Square roots in Eq. (9) cause no problems because N_i^2 and N_f^2 have always a positive real part. Consequently, following the theorem of analytic continuation, Eq. (6) also defines F for $V > V_{\text{lim}}$. In this way, one may calculate the radial matrix elements of resonance states which *a priori* are not normalizable.

B. Scattering states

Scattering states represent the nonresonant continuum and explicitly enter the completeness relations discussed in Sec III. Their asymptotic behavior at $r \rightarrow +\infty$ is

$$u(r) \sim C^+ H_{\ell, \eta}^{(+)}(kr) + C^- H_{\ell, \eta}^{(-)}(kr), \quad (12)$$

where $H_{\ell, \eta}^{(\pm)}$ denote Hankel (or Coulomb) functions. As usual, $u(r)$ is normalized to the Dirac δ distribution:

$$\int_0^{+\infty} \tilde{u}(k, r) u(k', r) dr = \delta(k - k'), \quad (13)$$

which gives

$$C^+ C^- = \frac{1}{2\pi}. \quad (14)$$

Knowing $u(r)$, $H_{\ell, \eta}^{(+)}$, $H_{\ell, \eta}^{(-)}$, and their derivatives at point R , one may determine coefficients C^+ and C^- up to a normalization factor by solving the set of linear equations:

$$u(R) = C^+ H_{\ell, \eta}^{(+)}(kR) + C^- H_{\ell, \eta}^{(-)}(kR), \quad (15)$$

$$u'(R) = kC^+ \left[\frac{dH_{\ell, \eta}^{(+)}}{dz} \right]_{z=kR} + kC^- \left[\frac{dH_{\ell, \eta}^{(-)}}{dz} \right]_{z=kR}.$$

Finally, the scattering state is normalized to satisfy condition (14).

C. Matrix elements involving scattering states

The calculation of matrix elements involving the scattering states is based on the complex rotation (9,10). However, the analytical continuation should be introduced differently than for resonant states. The one-body matrix element can be written as

$$\begin{aligned}
F(k_f) = & \int_0^R u_f(r) V(r) u_i(r) dr + A_f A_i F_{++}(k_f) \\
& + A_f B_i F_{+-}(k_f) + B_f A_i F_{-+}(k_f) + B_f B_i F_{--}(k_f),
\end{aligned} \tag{16}$$

where

- (i) $u_f = A_f u_f^+ + B_f u_f^-$;
- (ii) $u_i = A_i u_i^+ + B_i u_i^-$, where k_i in F is fixed and, in general, u_i can be either a bound, resonant or scattering state; and
- (iii) $F_{s_f s_i}(k_f) = \int_0^{+\infty} u_f^{s_f}(R+x) O(R+x) u_i^{s_i}(R+x) dx$ with $s_f, s_i \in (+, -)$.

This separation is necessary because the presence of incoming and outgoing waves in the same integral does not allow one to find a unique path in the complex plane along which the integrand decreases exponentially. Consequently, for each $F_{s_f s_i}$ one has to consider the domain of the complex plane where it converges, and then one performs an analytical continuation with the appropriate angle $\theta_{s_f s_i}$.

Certain integrals cannot be regularized in the above sense. Those include F_{+-} and F_{-+} with $u_i = u_f$. For $O(r) = 1$, the integrand tends toward a constant value at $+\infty$, independently of the value θ_{+-} . This can be immediately seen for neutrons, because with $z = R+x \cdot e^{i\theta}$ and with $|z| \rightarrow +\infty$, the product $u^+(z) \cdot u^-(z) \rightarrow \text{const} \times e^{ikz} \times e^{-ikz} = \text{const}$, and the corresponding integral diverges. In this case, however, it is easy to see that the integral is in fact a δ distribution, and it can be calculated by using a discrete representation of the Dirac δ function,

$$\delta(k - k_0) \rightarrow \frac{\delta_{k, k_0}}{\Delta k}, \tag{17}$$

with Δk being the discretization step in k .

III. COMPLETENESS RELATION INVOLVING SINGLE-PARTICLE GAMOW STATES

There exist several completeness relations involving resonant states. As shown by Lind [38], they all can be derived from Mittag-Leffler theory. In the following, we briefly discuss the Berggren completeness relation [34] which is used in our paper. The following discussion will concern the s.p. radial wave functions corresponding to a given partial wave (j, ℓ) .

We begin from the completeness relation of Newton [39]:

$$\sum_n |u_n\rangle \langle u_n| + \int_0^{+\infty} |u_k\rangle \langle u_k| dk = 1, \tag{18}$$

where $|u_n\rangle$ are the normalized bound states and $|u_k\rangle$ are the scattering states along the real energy axis normalized according to Eq. (13). In basis (18), one can expand any bound state or scattering state with *real energy*. Unfortunately, in the presence of narrow resonances, the discretization of the

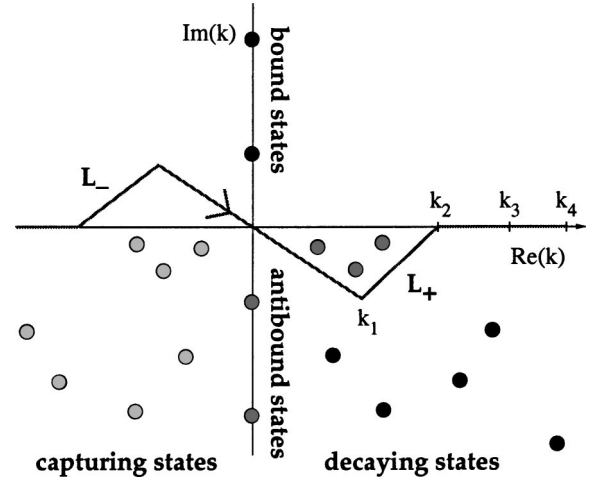


FIG. 2. Representation of the complex k plane, showing the positions of bound states, resonances, antiresonances, and the anti-bound states. L_+ is the contour representing the nonresonant continuum. The Berggren completeness relation involves the bound states, decaying states lying between L_+ and real k axis, and the scattering states on L_+ . The contour L_+ has to be chosen in such a way that all the poles in the discrete sum in Eq. (28) are contained in the domain between L_+ and the real energy axis.

real energy continuum becomes cumbersome. The complex-energy formalism of Gamow states offers a simple remedy to this difficulty.

In order to derive the completeness relation with Gamow states, one has to deform the integration contour into the complex k plane, as shown in Fig. 2. Following the residuum theorem, one obtains

$$\begin{aligned}
& - \int_0^{+\infty} |u_k\rangle \langle u_k| dk + \int_{L_+} |u_k\rangle \langle \tilde{u}_k| dk \\
& = 2i\pi \sum_{k_n} \text{Res}(|u_k\rangle \langle \tilde{u}_k|)_{k=k_n},
\end{aligned} \tag{19}$$

where k_n are the poles of $|u_k\rangle \langle \tilde{u}_k|$ lying between the real axis and the complex contour.

In general, the scattering wave function u_k can be written as

$$u_k(r) = \left(\frac{-\mathcal{J}^-(k)}{2\pi\mathcal{J}^+(k)} \right)^{1/2} u_k^+(r) + \left(\frac{-\mathcal{J}^+(k)}{2\pi\mathcal{J}^-(k)} \right)^{1/2} u_k^-(r). \tag{20}$$

In the above expression, \mathcal{J}^\pm stands for the Jost function [40]:

$$\mathcal{J}^\pm(k) = u^\pm \frac{du}{dr} - u \frac{du^\pm}{dr}, \tag{21}$$

where $u^\pm \sim H_{l, \eta}^\pm(kr)$ when $r \rightarrow +\infty$, and $u \equiv Au^+ + Bu^-$. For bound and decaying states, $\mathcal{J}^-(k) \neq 0$ ($\mathcal{J}^-(k) = 0$ only for capturing states with the incoming wave asymptotics). Consequently, the pole of $u_k(r)$ corresponds to zero of $\mathcal{I}^+(k)$. When $k \rightarrow k_n$, i.e., when u_k approaches the resonant state, then:

$$|u_k\rangle\langle\widetilde{u}_k|\sim -\frac{\mathcal{J}^-(k_n)}{2\pi\mathcal{J}^+(k)}|u_{k_n}^+\rangle\langle\widetilde{u}_{k_n}^+|, \quad (22)$$

$$\langle u_i|\widetilde{u}_j\rangle = \delta_{i,j}, \quad (30)$$

The derivative of the Jost function at $k=k_n$ is

$$\left[\frac{d\mathcal{J}}{dk}\right]_{k=k_n} = i\mathcal{J}^-(k_n)\text{Reg}\left[\int_0^{+\infty} u_{k_n}^{+2}(r)dr\right]. \quad (23)$$

As this derivative is nonzero, we have as $k\rightarrow k_n$,

$$\mathcal{J}^+(k)\sim(k-k_n)\left[\frac{d\mathcal{J}^+}{dk}\right]_{k=k_n}, \quad (24)$$

hence

$$|u_k\rangle\langle\widetilde{u}_k|\sim -\frac{1}{2\pi i(k-k_n)}|u_n\rangle\langle\widetilde{u}_n|, \quad (25)$$

where the normalized resonant state is

$$u_n(r) = u_{k_n}^+(r)\left(\text{Reg}\left[\int_0^{+\infty} u_{k_n}^{+2}(r)dr\right]\right)^{-1/2}. \quad (26)$$

Finally, the residuum at $k=k_n$ is

$$\text{Res}(|u_k\rangle\langle\widetilde{u}_k|)_{k=k_n} = -\frac{1}{2i\pi}|u_n\rangle\langle\widetilde{u}_n|, \quad (27)$$

and the completeness relation follows immediately:

$$\sum_n |u_n\rangle\langle\widetilde{u}_n| + \int_{L_+} |u_k\rangle\langle\widetilde{u}_k| dk = 1. \quad (28)$$

In the above equation $|u_n\rangle$ are the Gamow states (both bound states and the decaying resonant states between the real k axis and the complex contour). Relation (28) is the Berggren completeness relation which allows one to expand the states with complex k inside the zone between real k axis and the complex contour. One may notice again that the resonances in Eq. (26) are normalized using the squared wave function and not the modulus of the squared wave function. This is a consequence of the analytical continuation which is used to introduce the normalization of Gamow states.

Figure 2 illustrates the ingredients entering Eq. (28). The resonant states, the poles of the S matrix, are represented by the dots. They are divided into the bound, decaying, capturing, and antibound states (see, e.g., Refs. [34,41,38]). Relation (28) involves the bound and decaying states and the contour L_+ lying in the fourth quadrant of the complex- k plane.

In practical applications, one has to discretize the integral in Eq. (28) [42,43]:

$$\int_{L_+} |u_k\rangle\langle\widetilde{u}_k| dk \approx \sum_{i=1}^{N_d} |u_i\rangle\langle\widetilde{u}_i|, \quad (29)$$

where $u_i(r) = \sqrt{\Delta_{k_i}} u_{k_i}(r)$ and Δ_{k_i} is the discretization step. It follows from the definition of $u_i(r)$ that

and the discretized Berggren relation (28) takes the form

$$\sum_n |u_n\rangle\langle\widetilde{u}_n| + \sum_{i=1}^{N_d} |u_i\rangle\langle\widetilde{u}_i| \approx 1. \quad (31)$$

This relation is formally identical to the standard completeness relation in a discrete basis and, in the same way, leads to the eigenvalue problem $H|\Psi\rangle = E|\Psi\rangle$. However, as the formalism of Gamow states is non-hermitian, the matrix H is complex symmetric.

Up to this point, the choice of the contour in Eq. (2) has been completely arbitrary. In practice, however, one wants to minimize the number of discretization points N_d along L_+ . This can be achieved if the scattering functions on the contour (or, rather, their phase shifts) change smoothly from point to point. This condition can be met if the contour does not lie in the vicinity of a pole, especially the narrow resonant state. If this condition is met, the states appearing in basis (31) can be naturally divided into the following.

(i) *Bound states*—lying on the imaginary k axis (or negative real energy axis).

(ii) *Narrow decaying states*—lying close to and below the real k axis (or below the positive real energy axis). Those states can be interpreted as *physical resonances of the system*.

(iii) *Nonresonant continuum*—represented by the scattering states along L_+ . Physically, those are the building blocks of the nonresonant background.

These definitions can be extended to many-body states in the complex energy (or momentum) plane. In the following, we shall clearly distinguish between resonant, resonance, and nonresonant states.

The completeness relations derived above hold in every (j, ℓ) channel. Consequently, in practical calculations, one has to take different contours for different partial waves. As discussed below, the choice of the contour depends on the distribution of resonant states in the complex k -plane.

In a number of papers (see, e.g., Refs. [44–46]), resonant states were applied to problems involving continuum in the so-called *pole expansion*, neglecting the contour integral in Eq. (28). The importance of the contour contribution was investigated in Refs. [47,48,25–27] where it was concluded that if one is aiming at a detailed description, the nonresonant contribution must be accounted for. This point will be clearly seen in several examples discussed below.

Completeness of the one-body Berggren basis: illustrative examples

In this section, we shall discuss examples of the Berggren completeness relation in the one-body case. The s.p. basis is generated by the spherical Woods-Saxon (WS) potential:

$$V(r) = -V_0 f(r) - V_{s0} 4\vec{l} \cdot \vec{s} \frac{1}{r} \frac{df(r)}{dr}, \quad (32a)$$

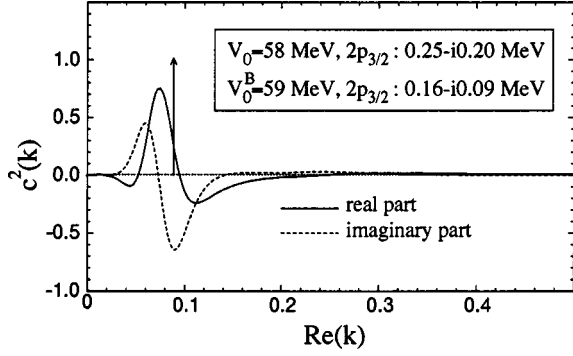


FIG. 3. Distribution of the squared amplitudes $c^2(k)$ of the s.p. state $2p_{3/2}$ of one WS potential ($V_0=58$ MeV) in the s.p. basis generated by another WS potential ($V_0^{(B)}=58$ MeV). The amplitudes of both real (solid line) and imaginary (dashed line) parts of the wave function are plotted as a function of $\text{Re}[k]$. The height of the arrow gives the squared amplitude of the $2p_{3/2}$ resonance contained in the basis.

$$f(r) = \left[1 + \exp\left(\frac{r-R_0}{d}\right) \right]^{-1}. \quad (32b)$$

In all examples of this section, the WS potential has the radius $R_0=5.3$ fm, diffuseness $d=0.65$ fm, and the spin-orbit strength $V_{so}=5.0$ MeV. The depth of the central part is varied to simulate different situations.

The complex contour corresponds to three straight segments in the complex k plane, joining the points: $k_0=0.0-i0.0$, $k_1=0.2-i0.2$, $k_2=0.5-i0.0$, and $k_3=2.0-i0.0$. The contour is discretized with a different number of points: $n=60, 80, 100, 120, 160$, and final results are obtained using the Richardson extrapolation method. In the examples considered in this section, we shall expand the $2p_{3/2}$ state, $|u_{\text{WS}}\rangle$, either weakly bound or resonant, in the basis $|u_{\text{WS}^B}(k)\rangle$ generated by the WS potential of a different depth:

$$|u_{\text{WS}}\rangle = \sum_i c_{k_i} |u_{\text{WS}^B}(k_i)\rangle + \int_{L_+} c(k) |u_{\text{WS}^B}(k)\rangle dk; \quad (33)$$

cf. Eq. (28). In the above equation, the first term in the expansion represents contributions from the resonant states while the second term is the nonresonant continuum contribution. Since the basis is properly normalized, the expansion amplitudes meet the condition

$$\sum_i c_{k_i}^2 + \int_{L_+} c^2(k) dk = 1. \quad (34)$$

In all cases considered, the $0p_{3/2}$ and $1p_{3/2}$ orbitals are well bound (by ~ 40 and ~ 18 MeV, respectively) and do not play any role in the expansion studied.

In the first example, we shall expand the $2p_{3/2}$ s.p. resonance ($0.25-i0.20$ MeV) of a WS potential of the depth $V_0=58$ MeV in the basis generated by the WS potential of the depth $V_0^B=59$ MeV (here the $2p_{3/2}$ s.p. resonance has an energy of $0.16-i0.09$ MeV). The density of the expansion

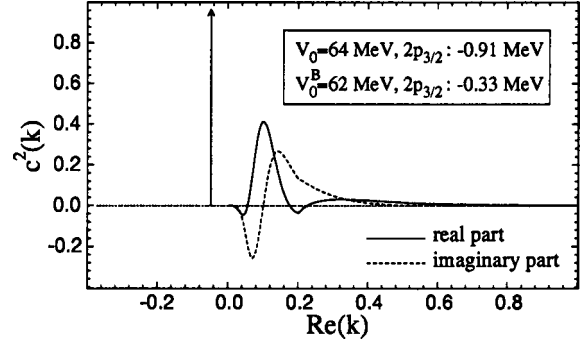


FIG. 4. Similar as in Fig. 3 but for the bound $2p_{3/2}$ s.p. state of the WS potential with $V_0=64$ MeV expanded in the basis generated by another WS potential ($V_0^{(B)}=62$ MeV). The height of the arrow gives the squared amplitude of the bound $2p_{3/2}$ state at the value of $\text{Im}[k]$ (the corresponding k value is purely imaginary).

amplitudes is shown in Fig. 3. One can see that the contribution from the nonresonant continuum is essential even though the $2p_{3/2}$ basis state is a resonance. In this example, as one might expect, the contribution from the resonance state in the basis is dominant.

The second example shown in Fig. 4 deals with the case of a $2p_{3/2}$ state that is bound in both potentials. Here $V_0=64$ MeV and $V_0^{(B)}=62$ MeV, and the $2p_{3/2}$ state lies at -0.91 and -0.33 MeV, respectively. As in the previous case, the contribution from the resonant (here: bound) state in the Berggren basis dominates and the contribution of the nonresonant continuum is small although nonnegligible. In this figure, one can notice the small cusp at $\text{Re}[k]=0.2$, even though the density $c^2(k)$ is an analytic function of k . This apparent paradox is due to the fact that $c^2(k)$ is plotted as a function of $\text{Re}[k]$ ($\text{Im}[k]=0$). Moreover, the path in the complex plane is continuous but not derivable at $k=0.2-i0.2$. These two aspects contribute to the appearance of the “discontinuous feature,” which of course has no physical meaning.

An interesting situation is presented in Fig. 5. Here the

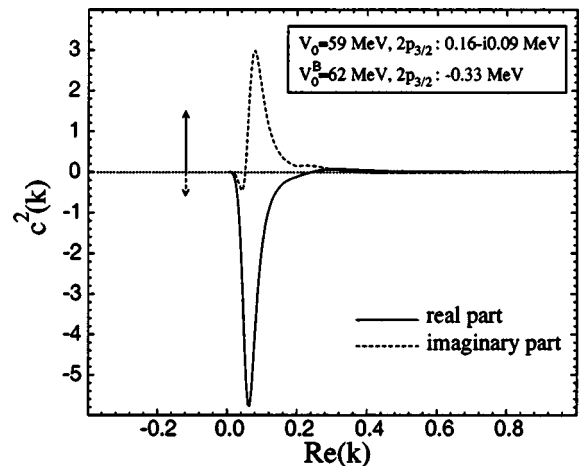


FIG. 5. Similar as in Fig. 3 except for the $2p_{3/2}$ resonance of the WS potential with $V_0=59$ MeV expanded in the basis generated by another WS potential ($V_0^{(B)}=62$ MeV).

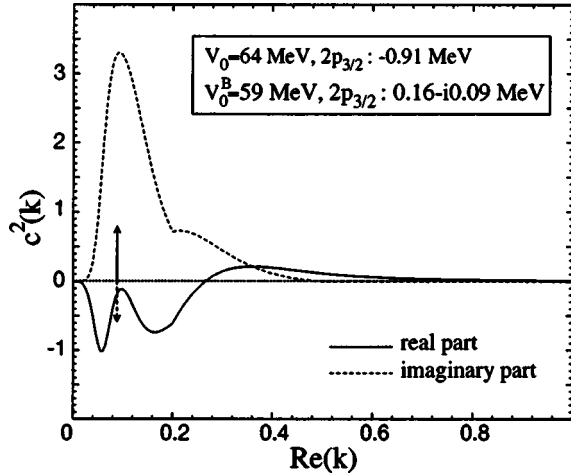


FIG. 6. Similar as in Fig. 3 except for the $2p_{3/2}$ bound state of the WS potential with $V_0 = 64$ MeV expanded in the basis generated by another WS potential ($V_0^B = 59$ MeV) containing a resonance.

unbound $2p_{3/2}$ state ($V_0 = 59$ MeV) is expanded in a WS basis containing the bound $2p_{3/2}$ level ($V_0^B = 62$ MeV). Consequently, the nonresonant continuum has to supply the imaginary part of the resonance's wave function. The last example (Fig. 6) corresponds to $V_0 = 64$ MeV and $V_0^B = 59$ MeV. This is the most intriguing case since one expresses a bound (real) state in the basis which contains only complex wave functions (the contribution from well bound $0p_{3/2}$ and $1p_{3/2}$ s.p. states is negligible). In this case, the nonresonant continuum annihilates the imaginary component of the $2p_{3/2}$ s.p. resonance contained in the basis. Indeed, in this example, the contribution from the contour is dominant. To see the convergence of the wave function obtained by the expansion method, in Fig. 7 we show the root-mean-square deviation of the calculated $2p_{3/2}$ wave function from the ex-

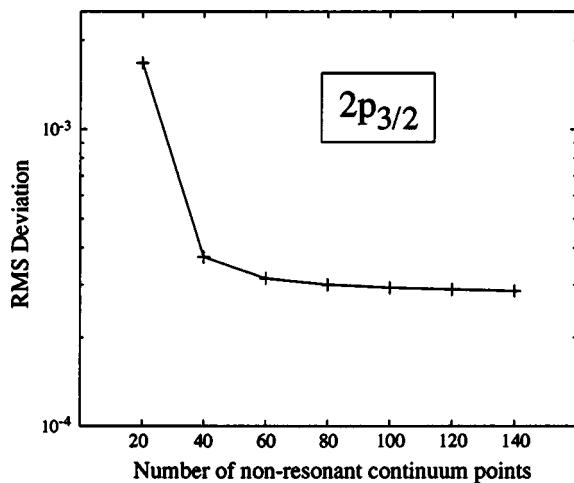


FIG. 7. The root-mean-square deviation of the $2p_{3/2}$ wave function of the WS potential ($V_0 = 64$ MeV) obtained by a diagonalization in a basis generated by another WS potential ($V_0^B = 59$ MeV) from the exact wave function (obtained by a direct integration of the Schrödinger equation). The rms deviation is shown as a function of the number of discretization points along the $2p_{3/2}$ contour.

TABLE I. Parameters of the GSM Hamiltonian used in the calculations for the oxygen isotopes (“ ^{17}O ” parameter set) and the helium isotopes (“ ^5He ” parameter set): WS radius R , WS diffuseness d , WS strength V_0 , spin-orbit strength V_{so} , and strength of the residual SDI interaction V_{SDI} .

Variant	R (fm)	d (fm)	V_0 (MeV)	V_{so} (MeV)	V_{SDI} (MeV fm ³)
^{17}O	3.05	0.65	55.8	6.06	700
^5He	2.00	0.65	47.0	7.50	1670

act result as a function of the number of discretization points along the contour. While the wave functions converge fairly quickly, the convergence of complex energies is slightly slower; hence, one has to employ the Richardson extrapolation method to get an energy precision of the order of a keV.

IV. GAMOW SHELL MODEL HAMILTONIAN

The GSM Hamiltonian applied in this work consists of a one-body term and a zero-range two-body interaction. The spherical one-body potential was taken in a WS form [Eq. (32a)]. In our study, resonant states are determined using the generalized shooting method for bound states which requires an exterior complex scaling. The numerical algorithm for finding Gamow states for any finite-depth potential has been tested on the example of the Pöschl-Teller-Ginocchio (PTG) potential [49], for which the resonance energies and wave functions are known analytically. Energies of all PTG resonances with a width of up to 90 MeV are reproduced with a precision of at least 10^{-6} MeV.

Contrary to the traditional shell model, the effective interaction of CSM cannot be represented as a single matrix calculated for all nuclei in a given region. The GSM Hamiltonian contains a real effective two-body force expressed in terms of space, spin, and isospin coordinates. The matrix elements involving continuum states are strongly system dependent, and they have to be determined for each case separately. This creates an additional difficulty, but there is also a payoff. Namely, the resulting two-body matrix elements fully take into account the spatial extension of s.p. wave functions.

In this work, as a residual interaction we took the surface delta interaction (SDI) [50]

$$V(1,2) = -V_{\text{SDI}} \delta(\vec{r}_1 - \vec{r}_2) \delta(r_1 - R), \quad (35)$$

with the same value of R as in the WS potential. In our exploratory GSM calculations, we consider two cases: (i) the chain of oxygen isotopes with the inert ^{16}O core and active neutrons in the sd shell, and (ii) the helium chain with the inert ^4He core and active neutrons in the p shell. The parameters of the GSM Hamiltonian are summarized in Table I. The WS potentials have been adjusted to s.p. states in one-neutron nuclei ^{17}O and ^5He . For ^{17}O , the resulting WS $0d_{5/2}$ and $1s_{1/2}$ states are bound, with s.p. energies of -4.142 and -3.272 MeV, respectively, and $0d_{3/2}$ is a resonance with the s.p. energy $0.898 - i0.485$ MeV. The agreement with experimental data ($e_{5/2_1^+}^{\text{expt}} = -4.143$ MeV, $e_{1/2_1^+}^{\text{expt}} = -3.273$ MeV, and $e_{3/2_1^+}^{\text{expt}} = 0.942$ MeV, $\gamma_{3/2_1^+}^{\text{expt}} = 96$ keV) is excellent. The strength

of the SDI has been adjusted for a given configuration space to the experimental two-neutron separation energy of ^{18}O . Since only $0d_{3/2}$ is a s.p. resonance, we shall include only a $d_{3/2}$ nonresonant continuum. In fact, the completeness relation requires taking the nonresonant continua corresponding to all partial waves (ℓ, j) . However, if for a given partial wave no resonances are included in the basis, the corresponding nonresonant continua can be chosen along the real momentum axis. Since, to the first order, the inclusion of these continua should only result in the renormalization of the effective interaction, they can be ignored in most cases, except for Sec. VB.

The nucleus ^5He with one neutron in the p shell, is unstable with respect to the neutron emission. Indeed, the $J^\pi = 3/2^-$ ground state of ^5He lies 890 keV above the neutron emission threshold and its neutron width is large, $\Gamma = 648$ keV. The first excited state, $1/2^-$, is a very broad resonance ($\Gamma = 5.57$ MeV) that lies 2.16 MeV above the threshold. Our WS potential yields single-neutron resonances $p_{3/2}$ and $p_{1/2}$ at $E = 0.745 - i0.32$ MeV and $E = 2.130 - i2.936$ MeV, respectively. In our model space we take resonances $0p_{3/2}$, $0p_{1/2}$, and the two associated complex continua $p_{3/2}$ and $p_{1/2}$. The strength of the SDI has been adjusted for a given configuration space to the experimental two-neutron separation energy of ^6He .

For the N -body problem, the Hamiltonian matrix contains one- and two-body matrix elements. The one-body part corresponds to s.p. energies of basis states and contributes only to diagonal matrix elements. In general, the calculation of two-body matrix elements is performed by splitting the radial integral into 16 terms corresponding to all different possible asymptotic conditions of s.p. wave functions. Then, each term is regularized separately by an appropriate choice of angle of the external complex scaling; cf. Sec. II.

V. MANY-BODY COMPLETENESS RELATION WITH GAMOW STATES

The discretized basis (31) can be a starting point for establishing the completeness relation in the many-body case, in a full analogy with the standard shell-model in a complete discrete basis, e.g., the harmonic oscillator basis. In this case one has

$$\sum_n |\Psi_n\rangle\langle\tilde{\Psi}_n| \approx 1, \quad (36)$$

where the N -body Slater determinants $|\Psi_n\rangle$ have the form $|\phi_1 \cdots \phi_N\rangle$, where $|\phi_k\rangle$ are resonance (bound and decaying) and scattering (contour) s.p. states. The approximate equality in Eq. (36) is an obvious consequence of the continuum discretization, similarly as in Eq. (31). Like in the case of s.p. Gamow states, the normalization of the Gamow vectors in the configuration space is given by the squares of shell-model amplitudes,

$$\sum_n c_n^2 = 1, \quad (37)$$

and not to the squares of their absolute values.

In the particular case of two-particle states, the completeness relation reads

$$\sum_{i_1, i_2} |\phi_{i_1} \phi_{i_2}\rangle_{JJ} \langle\phi_{i_1} \phi_{i_2}| \approx 1. \quad (38)$$

This relation can be used to calculate the two-body matrix elements.

A. Determination of many-body bound and resonance states

Before discussing completeness relations in the many-body case, let us describe the method of selecting many-body resonances. In a standard shell model, one often uses the Lanczos method to find the low-energy eigenstates (bound states) in very large configuration spaces. This popular method is unfortunately useless for the determination of many-body resonances because of a huge number (continuum) of surrounding many-body scattering states, many of them having lower energy than the resonances. A practical solution to this problem is the two-step procedure proposed in Ref. [25].

(i) In the first step, one performs the pole approximation, i.e., the Hamiltonian is diagonalized in a smaller basis consisting of s.p. resonant states only. Here, some variant of the Lanczos method can be applied. The diagonalization yields the first-order approximation to many-body resonances $|\Psi_i\rangle^{(0)}$, where index i ($i = 1, \dots, N$) enumerates all eigenvectors in the restricted space. These eigenvectors serve as starting vectors (pivots) for the second step of the procedure.

(ii) In the second step, one includes couplings to non-resonant continuum states in the Lanczos subspace generated by $|\Psi_j\rangle^{(0)}$ ($j \in [1, \dots, N]$).

(iii) Finally, one searches among the M solutions $|\Psi_{j;k}\rangle$ ($k = 1, \dots, M$) for the eigenvector which has the largest overlap with $|\Psi_j\rangle^{(0)}$.

This procedure is a variant of the Davidson method. Obviously, in the search for bound states, both Lanczos and Davidson methods can be used. In the following, we shall show that the procedure outlined above allows for an efficient determination of physical states within the set of all eigenvectors of a given Lanczos subspace.

As a representative example, let us consider the cases of ^{18}O and ^{20}O with the core of ^{16}O , i.e., two- and four-particle systems, respectively. Here we employ the complex $d_{3/2}$ contour corresponding to two segments defined by the points: $k_1 = 0 + i0$, $k_2 = 0.2 - i0.05$, and $k_3 = 0.4 - i0.0$. The contour is discretized with 17 and 9 points for ^{18}O and ^{20}O , respectively. From all the possible many-body configurations, we only keep the Slater determinants with an energy less than 5 MeV and with a width smaller than 1.7 MeV.

The results of calculations for the 0^+ states in ^{18}O are displayed in Fig. 8. In this case, one obtains two bound states. An eigenstate lying just close to the real energy axis just above the two-neutron threshold is a candidate for a resonance. Even though the width of this state is very small, only the overlap with the states calculated in the pole approximation can give the answer. Figure 9 shows the overlap

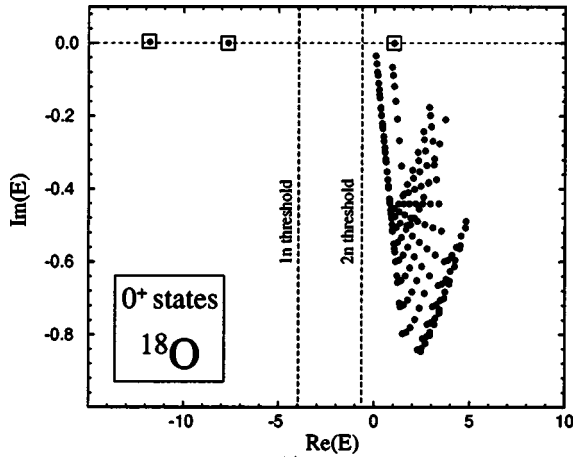


FIG. 8. Complex energies of the 0^+ states in ^{18}O resulting from the diagonalization of the GSM Hamiltonian. One- ($1n$) and two-neutron ($2n$) emission thresholds are indicated. The physical bound and narrow resonance states are marked by squares. The remaining eigenstates represent the nonresonant continuum.

of the ground-state wave function Ψ_0 of ^{18}O , calculated in the pole approximation, with all the 0^+ eigenstates of the GSM Hamiltonian resulting from the full diagonalization. One can see that only one state (the GSM ground state) has a significant overlap with Ψ_0 ; hence, the identification of the ground state wave function is unambiguous. Figure 10 illustrates a more challenging case of the third 0_3^+ state of ^{18}O . In spite of the fact that this state is embedded in the nonresonant 0^+ continuum, its identification is straightforward. It is interesting to notice that those GSM states in Fig. 8 that represent the nonresonant background tend to align along regular trajectories. As discussed in Refs. [26,27], the shapes of these trajectories directly reflect the geometry of the contour in the complex k plane. In the two-particle case, this

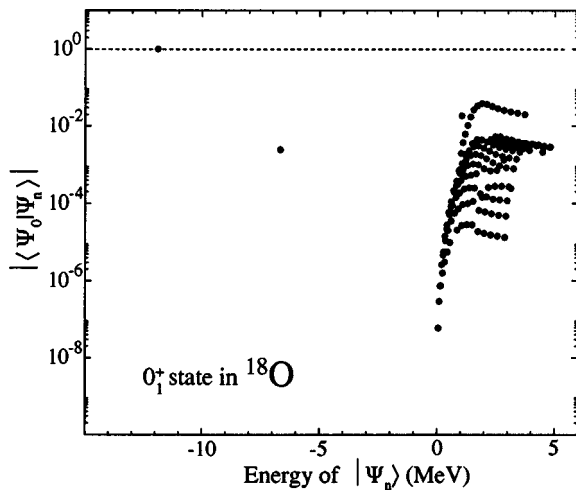


FIG. 9. Absolute value of the overlap between the ground state wave function Ψ_0 of ^{18}O calculated without the coupling to the nonresonant continuum (pole approximation) and the different 0_n^+ eigenstates Ψ_n of the GSM Hamiltonian (calculated with the couplings to the $d_{3/2}$ nonresonant continuum), as a function of the total energy.

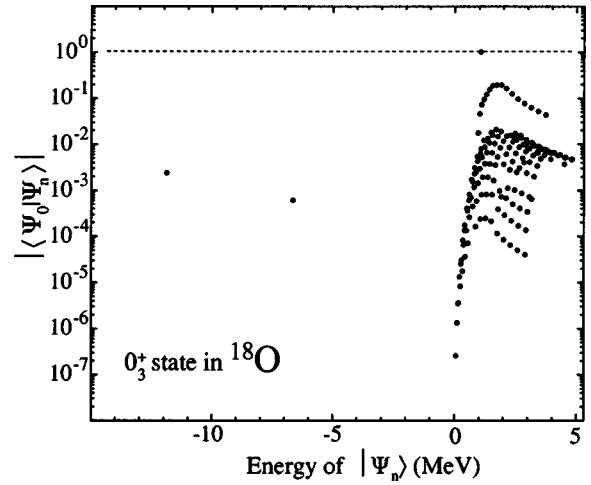


FIG. 10. Similar to Fig. 9 except for the 0_3^+ state wave function of ^{18}O , Ψ_3 .

information can be directly used to identify the resonance states.

Figure 11 shows the results of calculations for the 0^+ states in ^{20}O . As compared to the ^{18}O case, the number of many-body states is much larger and the regular pattern of nonresonant states reflecting the structure of the contour is gone (the figure represents the projection of four-dimensional trajectories onto two dimensional space). While the two lowest (bound) states can be simply identified by inspection, for the higher-lying states it is practically impossible to separate the resonances from the nonresonant continuum. However, the procedure outlined above makes it possible to identify unambiguously the many-body resonance states. On the other hand, the method proposed in Refs. [26,27] cannot be easily applied.

The many-body resonances should be stable with respect to small deformations of the contour (as the physical solutions should not be dependent on the deformation of the basis). This observation offers an independent criterion for

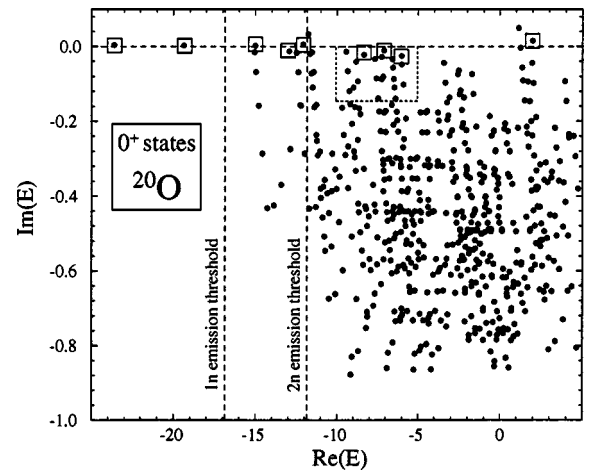


FIG. 11. Similar to Fig. 8 except for the 0^+ states in ^{20}O . The small negative widths of several unbound states are due to the fact that the number of discretization points along the contour is fairly small (5) in this case.

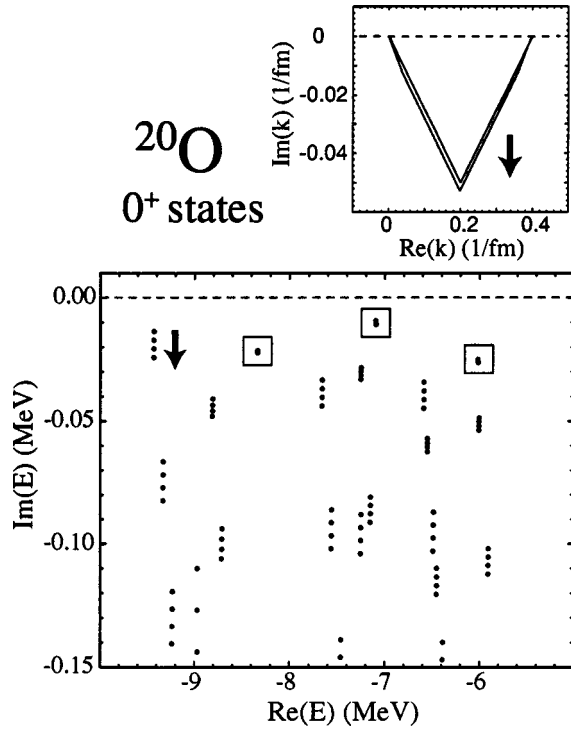


FIG. 12. The effect of small changes in the contour on the stability of resonant and nonresonant 0^+ states in ^{20}O . Top: the contour in the complex- k plane corresponding to the $0d_{3/2}$ continuum. The direction of the contour's deformation is indicated by an arrow. The calculations were performed for four contours, each divided into nine segments (i.e., ten discretization points); only the first and maximally deformed contours are shown. Bottom: the resulting shifts in positions of many-body states corresponding to the complex energy region of Fig. 11 marked by a dotted line. It is seen that the states identified as resonant are very stable with respect to small changes of the contour, while the states representing the nonresonant continuum move significantly in the direction indicated by an arrow.

identifying resonance states. Figure 12 shows the effect of a small deformation of the contour on the stability of selected 0^+ states in ^{20}O . As expected, only the states which have previously been identified as resonances are stable with respect to small changes of the contour; the states belonging to the nonresonant continuum “walk” in the complex energy plane following contour's motion.

B. Completeness of the many-body Gamow basis: example of two interacting particles

In this section, we shall discuss the completeness of the many-body basis spanned by Gamow states. Since the number of configurations is growing extremely fast with the number of valence nucleons, and this is enhanced by including the nonresonant continuum, we shall restrict our discussion to the case of two-valence particles. By analyzing the behavior of the wave function as the number of basis states grows, one can assess the impact of various truncations in the valence space. This is especially important for calculations with zero-range forces, such as the SDI interaction employed in this work, which require an energy cutoff. In the

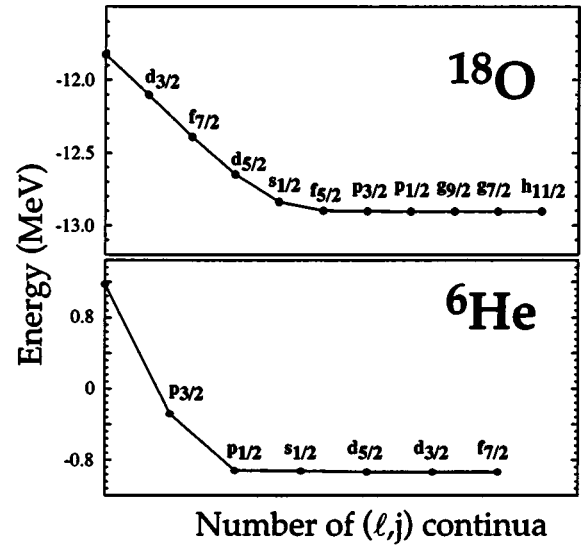


FIG. 13. Ground-state energy of ^{18}O (top) and ^6He (bottom) as a function of the number of different (ℓ, j) nonresonant continua in the valence space. For ^{18}O we employ the complex $d_{3/2}$ contour consisting of three straight segments connecting the points: $k_0 = 0.0 - i0.0$, $k_1 = 0.3 - i0.2$, $k_2 = 0.5 - i0$, and $k_3 = 1.3 - i0$ (all in fm^{-1}).

calculations contained in this section, the configuration space consists of all the Slater determinants of energy less than 35 MeV.

As a first example, we shall consider the convergence of the ground-state energy of ^{18}O with the increasing size of the nonresonant phase space. The GSM s.p. space consists of the $0d_{5/2}$, $1s_{1/2}$ orbitals and the $0d_{3/2}$ Gamow resonance. This discrete basis is supplemented by adding successive continua: $s_{1/2}$, $p_{1/2}$, $p_{3/2}$, ..., in the decreasing order of their importance. Since $0d_{3/2}$ is a resonance, a $d_{3/2}$ contour should be complex, and we take it according to Sec. V A. Other nonresonant continua are real and for their path we choose a straight segment with $0 < k < 1.3 \text{ fm}^{-1}$. The discretization of each continuum, whether real or complex, is made with 10 points.

As one can see in Fig. 13 (top), the convergence is achieved with the $d_{3/2}$, $f_{7/2}$, $d_{5/2}$, $s_{1/2}$, and $f_{5/2}$ contours; the contributions from all the remaining partial waves with $\ell > 3$ and $\ell = 1$ are practically negligible. As a rule of thumb, the continua which contribute most to the binding energy are those which are associated either with s.p. resonances in the basis or with weakly bound s.p. states. This is the case with the $0d_{5/2}$, $1s_{1/2}$, and $0d_{3/2}$ orbitals, and also with the $0f_{7/2}$ state which has an energy of +7.43 MeV and a width of 3.04 MeV. Even though this wide resonance is absent in the basis, it has nevertheless an indirect influence through the $f_{7/2}$ contour which “keeps memory” of its presence. One may notice that the presence of the (complex) $d_{3/2}$ contour affects not only the real part of the ground-state energy but also its imaginary part; the ground-state energy has a spurious width of $\sim -130 \text{ keV}$ in the pole approximation, and this width is reduced to $\sim -2 \text{ keV}$ when the $d_{3/2}$ (10-point) contour is added. The spurious width of the ground state remains stable when other (real) contours are added.

TABLE II. Squared amplitudes of different configurations in the ground states of two-neutron systems ^{18}O and ^6He . The sum of squared amplitudes of all Slater determinants, including n particles in the nonresonant continuum, is denoted by $L_+^{(n)}$. See the text for details.

Nucleus	Configuration	c^2
^{18}O	$0d_{5/2}^2$	$0.872 + i1.146 \times 10^{-4}$
	$1s_{1/2}^2$	$0.044 - i5.973 \times 10^{-6}$
	$0d_{3/2}^2$	$0.028 - i6.624 \times 10^{-3}$
	$L_+^{(1)}$	$0.042 + i4.709 \times 10^{-3}$
	$L_+^{(2)}$	$0.015 + i1.795 \times 10^{-3}$
^6He	$0p_{3/2}^2$	$0.891 - i0.811$
	$0p_{1/2}^2$	$0.004 - i0.079$
	$L_+^{(1)}$	$0.255 + i0.861$
	$L_+^{(2)}$	$-0.150 + i0.029$

The structure of the ground-state wave function of ^{18}O calculated with the full nonresonant continuum discussed in the context of Fig. 13 is given in Table II. One can see that the configuration with two neutrons in the $0d_{5/2}$ shell dominates; the remaining configurations, including those with one and two neutrons in the nonresonant continuum, contribute $\sim 15\%$ to the wave function. Imaginary parts of squared amplitudes are generally very small. This is due to the small width of the $0d_{3/2}$ resonance included in the basis.

As a second example, we shall investigate the energy convergence for the weakly bound ground state of ^6He . We shall assume that the structure of ^6He can be described in the full $0p$ shell with two valence neutrons. Since the GSM s.p. space consists of the $0p_{3/2}$, $0p_{1/2}$ Gamow resonances, the associated $p_{3/2}$ and $p_{1/2}$ nonresonant continua should be complex. Here, the $p_{3/2}$ contour consists of three straight segments connected at points: $k_0 = 0.0 - i0.0$, $k_1 = 0.3 - i0.35$, $k_2 = 0.5 - i0$, and $k_3 = 0.7 - i0$. In the $p_{1/2}$ nonresonant channel, straight lines join the points: $k_0 = 0.0 - i0.0$, $k_1 = 0.4 - i0.5$, $k_2 = 0.5 - i0$, and $k_3 = 0.7 - i0$. For all other contours we take a segment $[0:0.7] \text{ fm}^{-1}$ of the real k axis. The $p_{3/2}$ contour is discretized with 20 points. All other contours, including the complex $p_{1/2}$ contour, are discretized with ten points.

As seen in Fig. 13 (bottom), the full energy convergence is attained with $p_{3/2}$ and $p_{1/2}$ contours; other scattering waves with $\ell > 1$ are negligible. Coupling to the nonresonant $p_{3/2}$ and $p_{1/2}$ continua changes not only the ground-state energy but also its (spurious) width. In the pole approximation, the calculated ground state has a huge width of ~ -2 MeV, which is reduced to ~ -650 keV when the $p_{3/2}$ contour is added, and it reaches $\Gamma \sim -10$ keV when both $p_{3/2}$ and $p_{1/2}$ nonresonant continua are included. Contrary to the case of ^{18}O , the pole approximation is totally unreliable, and it does not even give a rough approximation to the energy and wave function of the ground state of ^6He . The main reason is that in this case one attempts to describe the bound state using the basis which does not contain any bound state and, therefore, the nonresonant continuum is essential for compensating for the resonance contribution. The analogous situation, dis-

TABLE III. Same as in Table II but only including the $d_{3/2}$ contour.

Configuration	c^2
$0d_{5/2}^2$	$0.935 + i1.836 \times 10^{-4}$
$1s_{1/2}^2$	$0.040 - i1.560 \times 10^{-5}$
$0d_{3/2}^2$	$0.021 - i4.973 \times 10^{-3}$
$L_+^{(1)}$	$3.913 \times 10^{-3} + i4.412 \times 10^{-3}$
$L_+^{(2)}$	$-1.002 \times 10^{-4} + i3.939 \times 10^{-4}$

cussed in the context of a one-body problem, can be found in Sec. III A (Fig. 6).

The structure of the ground-state wave function of ^6He including all the (ℓ, j) continua shown in Fig. 13, is shown in Table II. One can see that the configuration with two neutrons in the $0p_{3/2}$ shell dominates, though the imaginary part of the corresponding squared amplitude is almost equal in magnitude to the real part. The amplitude of the $0p_{1/2}^2$ configuration is small, whereas the contributions from one and two particles in the nonresonant continuum, $L_+^{(1)}$ and $L_+^{(2)}$, are almost equally important.

VI. GSM STUDY OF OXYGEN ISOTOPES

In this section we shall discuss the GSM results for a chain of oxygen isotopes with several valence neutrons ($N_{\text{val}} \geq 2$). In the calculations, we assume the core of ^{16}O . As discussed in Sec. IV, the valence neutrons are distributed over the $1s_{1/2}$ and $0d_{5/2}$ bound shells, the $0d_{3/2}$ Gamow resonance, and the discretized $d_{3/2}$ nonresonant continuum. The complex $d_{3/2}$ contour corresponds to two segments defined by the points: $k_1 = 0 + i0$, $k_2 = 0.2 - i0.05$, and $k_3 = 0.4 - i0.0$. It is discretized with nine points. Consequently, the discretized s.p. GSM space (31) consists of a total of 12 subshells on which valence neutrons are distributed. Let us reiterate that we also introduce the cutoff in the configuration space of the GSM. In this study, we shall include all Slater determinants with an energy (width) smaller than 5 MeV (1.7 MeV). Moreover, we shall take only Slater determinants with, at most, two neutrons in the nonresonant continuum. We have checked that configurations with a larger number of neutrons in the nonresonant continuum are of minor importance in all nuclei from ^{18}O to ^{22}O , and their contribution is $< 0.01\%$ in all cases studied. Our aim is not to give the precise description of actual nuclei (for this, one would need a realistic Hamiltonian and a larger configuration space), but rather to illustrate the method, its basic ingredients, and underlying features.

A. Ground states of oxygen isotopes

According to our calculations (see, e.g., Table III for ^{18}O), the ground-state wave functions of $^{18-22}\text{O}$ are dominated by the single shell model configuration $0d_{5/2}^{N_{\text{val}}}$ having a weight of 80–95%; the nonresonant continuum contribution is relatively small. A one-neutron continuum provides between 0.1% and 1% of the wave function, whereas a two-neutron

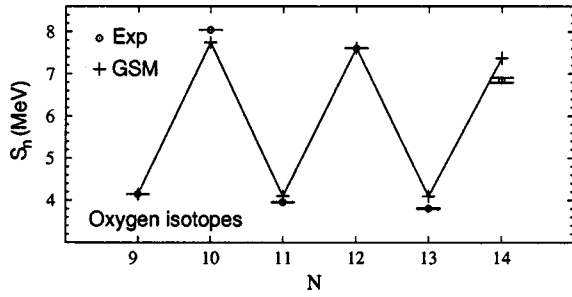


FIG. 14. Calculated (crosses connected by a solid line) and experimental (circles with error bars) one-neutron separation energies in the $^{18-22}\text{O}$ chain.

continuum yields a contribution which varies from $\sim 0.01\%$ to $\sim 0.1\%$ in these nuclei. This means that the main effect of the nonresonant continuum in these states is to cancel a spurious width induced by the $0d_{3/2}$ resonance included in the basis, and their influence on the real part of the energy can be neglected. It is interesting to compare the squared amplitudes for ^{18}O in Tables II and III. The values in Table II have been obtained by taking all the contours from $s_{1/2}$ to $h_{11/2}$, whereas the results in Table III have been calculated with only a $d_{3/2}$ contour. Increasing the nonresonant space gives rise to the depletion of the occupation of bound shells.

The predicted one-neutron separation energies S_n for oxygen isotopes are displayed in Fig. 14 and compared with the data. The calculations reproduce experimental separation energies, including the magnitude of the odd-even staggering. The difference between the GSM and the data are in the worst case ~ 500 keV.

B. Level schemes of oxygen isotopes

Shown in Figs. 15–17 are calculated and experimental spectra of $^{18-20}\text{O}$. Let us stress that the main purpose of this comparison is to demonstrate the internal coherence of GSM results and the numerical feasibility of the GSM in realistic applications. Nevertheless, in spite of the simplicity of the Hamiltonian, the overall agreement between the GSM and experimental spectra is quite reasonable.

Figure 15 illustrates the case of ^{18}O . One can see that the first three lowest states are relatively well described. Moreover, the one-neutron emission threshold is reproduced. In the GSM, this threshold is obtained from the difference of calculated ground-state energies of ^{18}O and ^{17}O . It is important to note that all states above the one-neutron emission threshold are predicted to be resonances, i.e., their widths are positive, whereas all states below this threshold are calculated to have small spurious negative widths. This feature is certainly not imposed on the model and it proves both an internal consistency of the GSM as well as a correct numerical account of the completeness for many-body Gamow states. One should notice that in the calculations with a discretized continuum, it is impossible to assure that the bound states have a width exactly equal to zero. Instead, one expects that this numerical artifact of continuum discretization becomes numerically unimportant with an increasing number of points on the contour (see Table 1 of Ref. [25]). With a

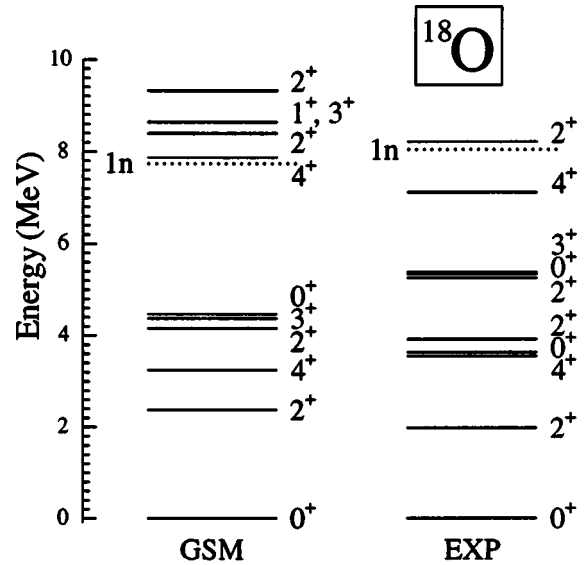


FIG. 15. The GSM level scheme of ^{18}O calculated in the full sd space of Gamow states and employing the discretized (ten points) $d_{3/2}$ nonresonant continuum. The dashed lines indicate experimental and calculated one-neutron emission thresholds. Experimental data are taken from Ref. [51].

ten-point discretization, the spurious width remains ~ -5 keV for all bound states of ^{18}O and we consider this a reasonable precision. Similarly, for resonances lying very close to the lowest particle emission threshold, hence having narrow widths, it may happen that their width results from the calculations as negative if the many-body completeness relation is numerically not well satisfied (see Fig. 11 and related discussion).

The calculated level scheme of ^{19}O (see Fig. 16) reproduces the main experimental features. The ground state is $5/2^+$, as observed, but the higher-lying states $3/2_1^+$ and $1/2_1^+$ are given in the reversed order. Nevertheless, the next four

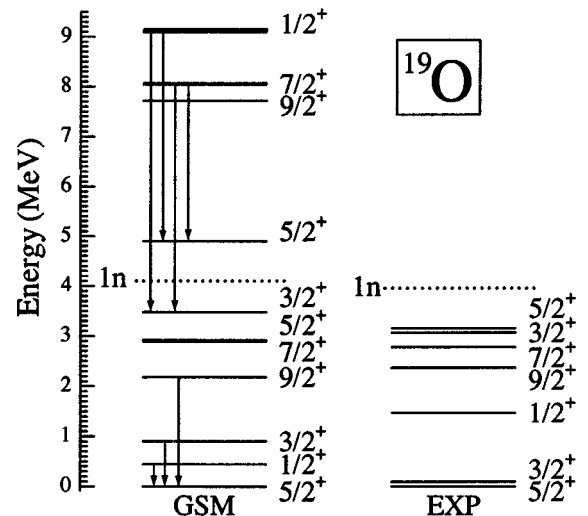
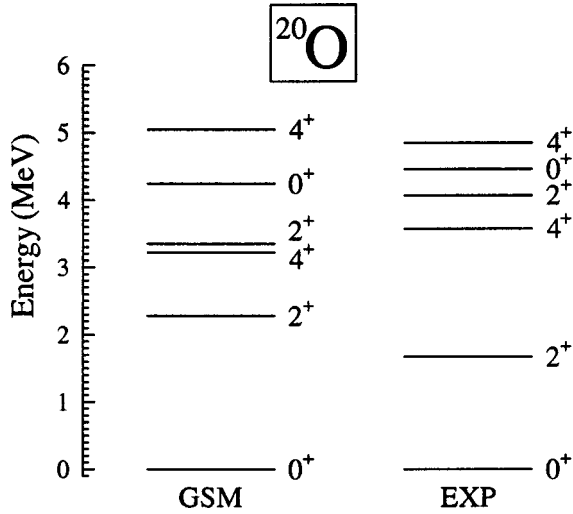


FIG. 16. Same as in Fig. 15 except for ^{19}O . As the number of states becomes large above the one-neutron emission threshold, only selected resonances are shown. The electromagnetic transitions listed in Table V are indicated by arrows.


 FIG. 17. Same as in Fig. 15, except for ^{20}O .

states are rather well reproduced, in spite of the inversion of the $5/2_2^+$ and $3/2_2^+$ levels. Finally, the GSM prediction for ^{20}O is shown in Fig. 17. Here, the overall agreement between calculations and experiment is best for all the isotopes studied.

C. Distribution of valence particles

Radial features of the density distribution of valence nucleons are always of great theoretical interest. They determine the nuclear size, electromagnetic transition rates, polarization charges, and many other nuclear properties. To assess the radial extent of the nucleonic distribution obtained in the GSM, we investigate the monopole form factor defined through the normalized radial Gamow wave functions $u_i(r)$ [Eq. (26)]:

$$\rho(r) = \sum_i n_i |u_i(r)\rangle \langle \tilde{u}_i(r)|, \quad (39)$$

where $n_i \equiv \langle a_n^+ a_n \rangle$ is the GSM occupation coefficient of the s.p. Gamow orbital i . By definition, the form factor is normalized to the number of valence particles:

$$\text{Reg} \int_{r=0}^{\infty} \rho(r) dr = N_{\text{val}}. \quad (40)$$

Figure 18 shows the neutron form factors for the ground state and the highly excited resonance state 2_5^+ of ^{18}O . As for all observables associated with bound states, the neutron form factor in the ground state of ^{18}O is real even though the $0d_{3/2}$ resonant state is included in the basis. The imaginary part of $\rho(r)$ is very small; its value is less than 3×10^{-5} for all values of r . On the other hand, for the 2_5^+ resonance, having a width of ~ 150 keV, the form factor is always complex. This feature is not an artifact of the discretization procedure. In fact, the imaginary part of the form factor has an interesting physical interpretation. Namely, it is associated with the uncertainty in the determination of the mean value (given by the real part) [30,34,52–54]. In other words, in the decaying state the particle distribution cannot be given with an unlimited precision.

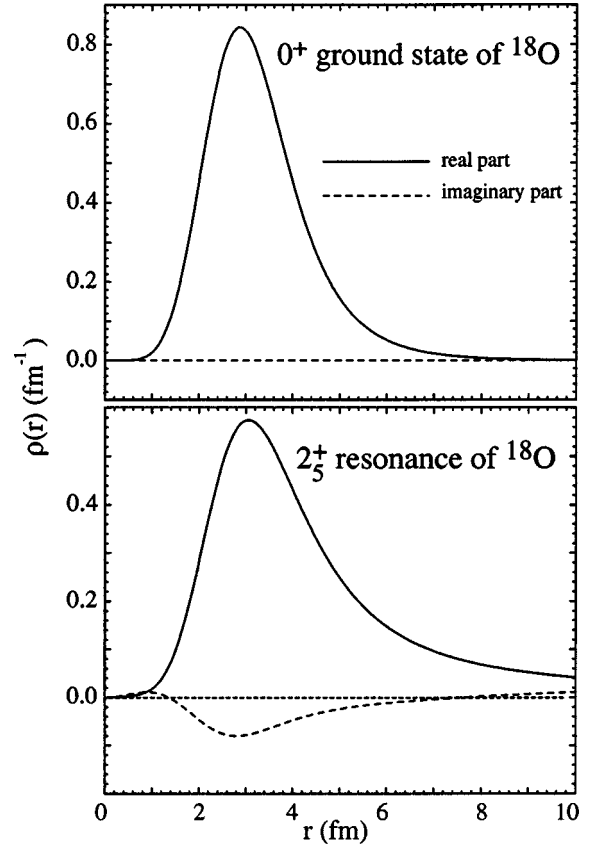


FIG. 18. Monopole form factor of valence neutrons [Eq. (39)] in the ground state (top) and the 2_5^+ resonance (bottom) of ^{18}O . Real and imaginary parts of the density are shown with solid and dotted lines, respectively. According to definition (40), the form factor is expressed in units of fm^{-1} .

D. Electromagnetic transition probabilities

In the shell-model calculations with Gamow states, only radial matrix elements are treated differently as compared to the standard shell model. This means that the electromagnetic (EM) transition selection rules and the angular momentum and isospin algebra do not change. To calculate the EM transitions, one can no longer use the long wavelength approximation because of the presence of the nonresonant continuum. Indeed, for the diagonal EM matrix elements $\langle n_i l_i j_i k_i | O | n_f l_f j_f k_f \rangle$ ($k_i = k_f$) between the scattering states, the complex scaling cannot be carried out [see the discussion around Eq. (17)]. Furthermore, since in the long wavelength approximation the EM operators behave like r^λ , one has to deal with derivatives of delta functions, which is difficult to handle. Without the long wavelength approximation, however, these matrix elements become finite, because it is always possible to carry out a complex scaling with the Bessel function of the photon $j_L(qr)$, as $q \neq 0$. Moreover, as they represent a set of measure zero, the diagonal nonresonant EM matrix elements can be put to zero in the discretized calculation. As all the other matrix elements can be regularized, the EM matrix elements are all well defined.

TABLE IV. Electromagnetic GSM rates (all in W.u.) for the selected transitions in ^{18}O calculated (i) in the pole approximation without the complex-energy contour and (ii) with the $d_{3/2}$ contour representing the nonresonant continuum. Experimental data [51] are shown in the last column.

Transition	Without contour	With contour	Expt.
$2_1^+ \rightarrow 0_1^+$ $E2$	$2.75 - i0.001$	$2.68 - i0.011$	3.32
$4_1^+ \rightarrow 2_1^+$ $E2$	$1.99 + i0.015$	$1.94 - i0.003$	1.19
$0_2^+ \rightarrow 2_1^+$ $E2$	$1.66 + i0.007$	$1.48 + i0.006$	17
$2_2^+ \rightarrow 2_1^+$ $M1$	$0.04 - i0.000$	$0.04 - i0.000$	0.14
$2_2^+ \rightarrow 0_1^+$ $E2$	$0.19 + i0.004$	$0.18 - i0.001$	1.3

Tables IV and V display the selected EM transition rates in ^{18}O and ^{19}O calculated in the GSM with and without the contribution from the nonresonant $d_{3/2}$ continuum. In all calculations, we have taken the effective neutron charge $\delta e_n = 0.5e$. While the radial form factor discussed in Sec. (VIC) determines the structure of monopole operators, the EM probabilities probe the off-diagonal matrix elements; hence the continuum coupling manifests itself differently. As seen in Tables IV and V, the nonresonant continuum plays an important role both for transitions involving bound states only and for transitions involving an unbound state or states. In all cases, the real part of the transition rate is reasonably approximated in the pole approximation.

Similarly as in the problem of spurious negative widths of bound states, the imaginary part of EM transitions between bound states must disappear in the limit of the nondiscretized continuum. Indeed, in our calculations the imaginary part of such a transition rate tends to zero when the coupling to the nonresonant continuum is added. In the cases studied, taking

TABLE V. Same as in Table IV except for electromagnetic transitions in ^{19}O shown in Fig. 16.

Transition	Without contour	With contour	Expt.
$3/2_1^+ \rightarrow 5/2_1^+$ $M1$	$0.01 - i0.002$	$0.01 - i0.0$	0.088
$1/2_1^+ \rightarrow 3/2_1^+$ $M1$	$0.02 - i0.003$	$0.02 + i0.0$	0.0093
$1/2_1^+ \rightarrow 5/2_1^+$ $E2$	$3.07 + i0.010$	$3.07 + i0.003$	0.58
$9/2_1^+ \rightarrow 5/2_1^+$ $E2$	$1.78 + i0.000$	$1.74 - i0.006$	<1
$7/2_3^+ \rightarrow 5/2_3^+$ $E2$	$0.12 - i0.062$	$0.13 - i0.037$	
$1/2_3^+ \rightarrow 5/2_3^+$ $E2$	$4.57 + i0.430$	$4.58 + i0.373$	
$7/2_3^+ \rightarrow 3/2_2^+$ $E2$	$0.12 + i0.038$	$0.13 + i0.054$	
$1/2_3^+ \rightarrow 3/2_2^+$ $E2$	$0.82 - 0.034$	$0.85 - i0.012$	

TABLE VI. Discretized $p_{3/2}$ and $p_{1/2}$ contours in the complex- k plane (in fm^{-1}) representing the nonresonant continuum in the He calculation.

Point No.	$p_{3/2}$	$p_{1/2}$
1	$0.01 - i0.01$	$0.05 - i0.05$
2	$0.10 - i0.06$	$0.20 - i0.43$
3	$0.20 - i0.095$	$0.40 - i0.45$
4	$0.30 - i0.06$	$0.60 - i0.43$
5	$0.40 - i0.01$	$0.75 - i0.05$

only ten points on the $d_{3/2}$ contour decreases the imaginary part by one to two orders of magnitude, depending on the transition. The real part of the transition probabilities changes by up to $\sim 10\%$ when the contribution from the contour is considered. This is nevertheless an important change if one notices that the configurations with one and two neutrons in the nonresonant continuum amount to $\sim 0.1\%$ of bound wave functions in these nuclei. For most transitions, the experimental values are reproduced within a factor of 3 by the GSM, and we find this agreement satisfactory in light of a very simple Hamiltonian employed.

Table V displays transition rates in ^{19}O , indicated in Fig. 16 by arrows. The three lowest transitions are between bound states and the GSM calculations with contour predict a very small imaginary part (less than 0.001 W.u.). The next four transitions in Table V involve the unbound $7/2_2^+$, $1/2_2^+$, and $5/2_3^+$ levels lying above the one-neutron threshold, and the corresponding transition rates are, in general, complex. The

effect is particularly pronounced for the $1/2_2^+ \rightarrow 5/2_3^+$ transition between unbound states. As mentioned in Sec. VIC, the imaginary part gives the uncertainty of the average value [30,53,54]. In all cases, the real part of the matrix element is slightly influenced by the interference with the nonresonant background.

VII. GSM STUDY OF HELIUM ISOTOPES

A description of the neutron-rich helium isotopes, including Borromean nuclei $^{6,8}\text{He}$, is a challenge for the GSM. ^4He is a well-bound system with the one-neutron emission threshold at 20.58 MeV. On the contrary, as discussed in Sec. IV, the nucleus ^5He is a broad resonance. The two-neutron system ^6He , on the contrary, is bound with the two-neutron emission threshold at 0.98 MeV and one-neutron emission threshold at 1.87 MeV. The first excited state 2_1^+ at 1.8 MeV in ^6He is neutron unstable with a width $\Gamma = 113$ keV.

The s.p. configuration space used includes both resonances $0p_{3/2}$, and $0p_{1/2}$ and the two associated complex continua $p_{3/2}$ and $p_{1/2}$, which are discretized with five points each. The fact that the resonances in the basis are so broad requires particular attention when selecting points along the contour. They are given in Table VI. In this case, we cannot significantly increase the density of points along the contour because the calculation for the heavier helium isotopes with more valence neutrons would not be feasible. On the other hand, we do not introduce any restriction on energies and

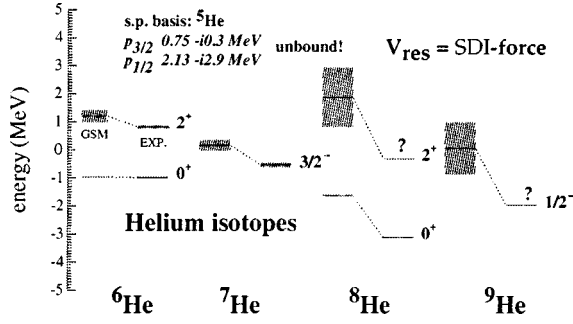


FIG. 19. Experimental (EXP) and predicted (GSM) binding energies of ${}^6\text{--}9\text{He}$ as well as energies of $J^\pi=2^+$ states in ${}^6,8\text{He}$. The resonance widths are indicated by shading. The energies are given with respect to the core of ${}^4\text{He}$.

widths of Slater determinants included. Also, no restriction on the number of neutrons in the nonresonant continuum is imposed, with the only exception being ${}^9\text{He}$, where we allow for at most four neutrons to occupy “contour shells.” Contrary to the discussion in Sec. V B, we neglect all remaining real continua in the present calculation. We shall see that this will have an impact on the relative weight of different configurations in the wave function.

A. Spectra of helium isotopes

The energies of the lowest GSM states of helium isotopes are shown in Fig. 19, and the structure of their ground state wave functions is given in Table VII. As seen in Table VII, the nonresonant continuum contributions $L_+^{(n)}$ are always essential, and, in some cases (e.g., ${}^8,9\text{He}$), they dominate the structure of the ground-state wave function. Moreover, as can be seen in the example of ${}^8\text{He}$, configurations with many neutrons in the nonresonant continuum are essential for fulfilling the completeness relation. In this particular case, the $L_+^{(1)}$ contribution is even more important than the contribution from the resonant states, and even the $L_+^{(4)}$ configuration gives a non-negligible contribution of the order of 1–2%. ($L_+^{(n)}$ amplitudes seem to decrease with n .) Without the contour, the predicted ground-state energy of ${}^8\text{He}$ is +2.08 MeV and the spurious width is huge, $\Gamma = -4.16$ MeV. The inclusion of scattering states lowers the binding energy to -1.6 MeV. Clearly, the pole approximation fails miserably in this case.

It is instructive to compare the wave function decomposition in Tables VII (only $p_{3/2}$ and $p_{1/2}$ contours are included) and II (all contours up to $f_{7/2}$ are included). As expected, the spread of the ground-state wave function over nonresonant continuum states is larger in the latter case, but this effect is relatively less important than in the case of ${}^{18}\text{O}$ (cf. Fig. 13).

Our calculations reproduce the most important feature of ${}^6\text{He}$ and ${}^8\text{He}$: *the ground state is particle bound, despite the fact that all the basis states lie in the continuum*. In spite of a very crude Hamiltonian, rather limited configuration space, etc., the calculated ground state energies shown in Fig. 19 reproduce surprisingly well the experimental data. The odd- N isotopes of ${}^7,9\text{He}$ are calculated to be neutron resonances. The neutron separation energy anomaly (i.e., the in-

TABLE VII. Squared amplitudes of different configurations in the ground states of ${}^6\text{--}9\text{He}$. The s.p. space consists of both $0p_{3/2}$, $0p_{1/2}$ Gamow resonances and the two associated complex continua $p_{3/2}$ and $p_{1/2}$ which are discretized with five points each.

Nucleus	Configuration	c^2
${}^6\text{He}$	$0p_{3/2}^2$	$0.870 - i0.736$
	$0p_{3/2}^2$	$0.007 - i0.076$
	$L_+^{(1)}$	$0.271 + i0.752$
	$L_+^{(2)}$	$-0.147 + i0.060$
${}^7\text{He}$	$0p_{3/2}^3$	$1.110 - i0.879$
	$0p_{3/2}^2 0p_{1/2}$	$0.006 - i0.029$
	$0p_{3/2} 0p_{1/2}^2$	$0.022 - i0.042$
	$L_+^{(1)}$	$0.050 + i0.951$
	$L_+^{(2)}$	$-0.185 + i0.008$
${}^8\text{He}$	$L_+^{(3)}$	$-0.002 - i0.009$
	$0p_{3/2}^4$	$0.296 - i1.323$
	$0p_{3/2}^2 0p_{1/2}^2$	$-0.060 - i0.158$
	$L_+^{(1)}$	$1.596 + i1.066$
	$L_+^{(2)}$	$-0.728 + i0.630$
${}^9\text{He}$	$L_+^{(3)}$	$-0.125 - i0.204$
	$L_+^{(4)}$	$0.020 - i0.012$
	$0p_{3/2}^4 0p_{1/2}$	$0.180 - i1.328$
	$L_+^{(1)}$	$1.596 + i0.734$
	$L_+^{(2)}$	$-0.584 + i0.801$
	$L_+^{(3)}$	$-0.217 - i0.193$
	$L_+^{(4)}$	$0.025 - i0.034$

crease of one-neutron separation energy when going from ${}^6\text{He}$ to ${}^8\text{He}$) is reproduced. One can see that ${}^8\text{He}$ is predicted to be better bound than ${}^6\text{He}$, though, contrary to the data, the two-neutron separation energy of ${}^8\text{He}$ is smaller than that of ${}^6\text{He}$. Also, the energies of excited 2_1^+ states are in fair agreement with the data.

The present calculations for helium isotopes have a systematic tendency to underbind. The spurious width of the ground state of ${}^8\text{He}$ is ~ 100 keV, largely due to the $0p_{3/2}$ resonance. For that reason, the removal of the spurious width (which reflects the accuracy of our calculations) cannot be done here as precisely as in the oxygen case. In order to check the stability of the results for ${}^6,8\text{He}$, we carried out additional calculations increasing the number of points along the complex contour. We have found that the value of the two-neutron separation energy difference, $S_{2n}({}^8\text{He}) - S_{2n}({}^6\text{He})$, which is negative with 5 states in each nonresonant continuum, depends sensitively on the number of discretization points. This is because $S_{2n}({}^8\text{He})$ increases fast with the size of the nonresonant phase space. While with our schematic Hamiltonian we were unable to find a fully satisfactory result for the ground-state energy of ${}^8\text{He}$ just by increasing the number of discretization points, we can see that there is a systematic improvement when the number of nonresonant shells increases. Therefore, one would be tempted to associate the so-called “helium anomaly” in the position of two-neutron emission threshold when going from ${}^6\text{He}$ to

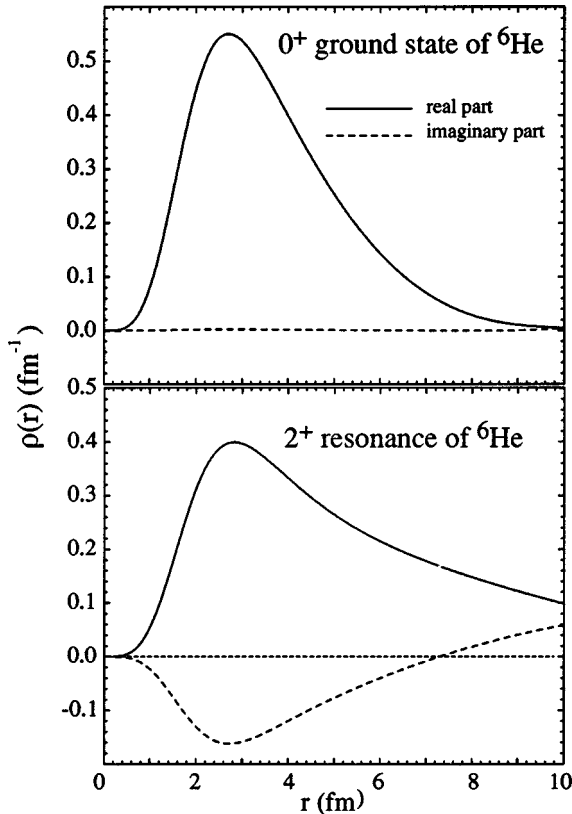


FIG. 20. Monopole form factor of valence neutrons for the ground state (top) and for the lowest 2_1^+ resonance (bottom) of ${}^6\text{He}$.

${}^8\text{He}$ with the strong enhancement in the occupation of non-resonant continuum states.

B. Distribution of valence neutrons in ${}^6\text{He}$

Form factors of valence neutrons [Eq. (39)] in 0_1^+ and 2_1^+ states of ${}^6\text{He}$ are shown in Fig. 20. In this calculation, we have taken discretized $p_{1/2}$ and $p_{3/2}$ continua with 20 points each. Even with this very high number of continuum states, the imaginary part of the form factor in the ground state of ${}^6\text{He}$ is still $\sim 2 \times 10^{-3} \text{ fm}^{-1}$. It is interesting to see that the radial distribution of neutrons in this case extends well above the range of the one-body potential, as expected for a weakly bound system. In the case of the first excited (resonance) 2_1^+ state, $\rho(r)$ is complex; real and imaginary parts of the density are of a comparable size, which is obviously related to the large width ($\sim 500 \text{ keV}$) of this state.

VIII. SUMMARY

This paper contains a detailed description of the Gamow shell model, which can be viewed as a straightforward extension of the standard diagonalization shell model that allows for a consistent treatment of bound states and the particle continuum, including both resonances and the nonresonant background. Our first application, based on a realistic, albeit simple, two-body SDI force, concerns many-neutron systems, including states and nuclei near the neutron-emission threshold.

In this work, we succeeded in overcoming several obstacles which traditionally plagued previous continuum shell model applications. In addition to the successful inclusion of the continuum-continuum coupling by means of the complex rotation technique (exterior complex scaling), we incorporated the nonresonant part of the continuum. This has been achieved by discretizing the contour in the complex k plane for each partial wave. Another problem which has been solved in our study is the isolation of resonance states. As a result of the GSM diagonalization, one obtains a multitude of states corresponding to the many-body continuum, some being resonances and some representing the nonresonant background. Our work offers a simple prescription on how to identify the resonance states from the multitude of complex-energy eigenstates of the GSM Hamiltonian.

The GSM Hamiltonian is composed of a one-body term and a two-body residual interaction which is directly written in terms of space, spin, and isospin coordinates. The two-body matrix elements have to be determined separately for each case by means of radial integration. As a result, the resulting Hamiltonian matrix fully takes into account the continuum coupling, in particular the spatial extension of s.p. wave functions, determining the physics of halo nuclei.

We demonstrated that the contribution from the nonresonant continuum is essential, especially for unbound and near-threshold states. In some cases (e.g., ${}^8,9\text{He}$) nonresonant continuum components dominate the structure of the ground state wave function. The so-called ‘‘pole approximation’’ (resonant state expansion) breaks down in such cases. In addition, the inclusion of the nonresonant continuum also impacts results for bound states.

The results of our first calculations for binding energies, spectra, electromagnetic matrix elements, and nucleonic distributions are very encouraging. In particular, pairing correlations due to the continuum-continuum scattering can bind the ground states of ${}^6,8\text{He}$ with a completely unbound basis provided by the s.p. resonances of ${}^5\text{He}$. The ‘‘helium anomaly’’ (an *increase* in one- and two-neutron separation energy when going from ${}^6\text{He}$ to ${}^8\text{He}$) is explained in terms of the neutron scattering to the nonresonant background. In all cases considered, our calculations yield neutron resonances above the calculated neutron threshold—a property that is not guaranteed *a priori* by the formalism.

Other applications of the GSM, including the case of open proton *and* neutron shells, also employing more realistic effective interactions, are in progress. We are also working on the optimization of the nonresonant part of calculations (choice of the contours, distribution of discretization points, etc.). We are convinced that the Gamow shell model will become a very useful theoretical tool unifying structure and reaction aspects of weakly bound nuclei.

ACKNOWLEDGMENTS

This work was supported in part by the U.S. Department of Energy under Contract Nos. DE-FG02-96ER40963 (University of Tennessee) and DE-AC05-00OR22725 with UT-Battelle, LLC (Oak Ridge National Laboratory).

- [1] J. Dobaczewski and W. Nazarewicz, *Philos. Trans. R. Soc. London, Ser. A* **356**, 2007 (1998).
- [2] E. Caurier, F. Nowacki, and A. Poves, *Eur. Phys. J. A* **15**, 145 (2002).
- [3] E. Caurier and G. Martinez-Pinedo, *Nucl. Phys.* **A704**, 60c (2002).
- [4] T. Otsuka, Y. Utsuno, R. Fujimoto, B. A. Brown, M. Honma, and T. Mizusaki, *Eur. Phys. J. A* **13**, 69 (2002); **15**, 151 (2002).
- [5] L. Coraggio, A. Covello, A. Gargano, N. Itaco, T. T. S. Kuo, D. R. Entem, and R. Machleidt, *Phys. Rev. C* **66**, 021303 (2002).
- [6] B. A. Brown, *Nucl. Phys.* **A704**, 11c (2002).
- [7] R. G. Thomas, *Phys. Rev.* **81**, 148 (1951); **88**, 1109 (1952).
- [8] J. B. Ehrman, *Phys. Rev.* **81**, 412 (1951).
- [9] H. Feshbach, *Ann. Phys. (N.Y.)* **19**, 287 (1962).
- [10] U. Fano, *Phys. Rev.* **124**, 1866 (1961).
- [11] C. Mahaux and H. Weidenmüller, *Shell Model Approaches to Nuclear Reactions* (North-Holland, Amsterdam, 1969).
- [12] H. W. Bartz, I. Rotter, and J. Höhn, *Nucl. Phys.* **A275**, 111 (1977); **A307**, 285 (1977).
- [13] R. J. Philpott, *Nucl. Phys.* **A289**, 109 (1977).
- [14] D. Halderson and R. J. Philpott, *Nucl. Phys.* **A345**, 141 (1980).
- [15] I. Rotter, *Rep. Prog. Phys.* **54**, 635 (1991), and references therein.
- [16] J. Okołowicz, M. Płoszajczak, and I. Rotter, *Phys. Rep.* **374**, 271 (2003).
- [17] K. Bennaceur, F. Nowacki, J. Okołowicz, and M. Płoszajczak, *Nucl. Phys.* **A651**, 289 (1999).
- [18] K. Bennaceur, N. Michel, F. Nowacki, J. Okołowicz, and M. Płoszajczak, *Phys. Lett.* **488B**, 75 (2000).
- [19] K. Bennaceur, F. Nowacki, J. Okołowicz, and M. Płoszajczak, *Nucl. Phys.* **A671**, 203 (2000).
- [20] B. V. Danilin, I. J. Thompson, J. S. Vaagen, and M. V. Zhukov, *Nucl. Phys.* **A632**, 383 (1998).
- [21] E. Nielsen, D. V. Fedorov, A. S. Jensen, and E. Garrido, *Phys. Rep.* **347**, 373 (2001).
- [22] H. Esbensen and G. F. Bertsch, *Phys. Rev. C* **59**, 3240 (1999).
- [23] D. Eppel and A. Lindner, *Nucl. Phys.* **A240**, 437 (1975).
- [24] W. M. Wandler, *Nucl. Phys.* **A472**, 26 (1987).
- [25] N. Michel, W. Nazarewicz, M. Płoszajczak, and K. Bennaceur, *Phys. Rev. Lett.* **89**, 042502 (2002).
- [26] R. Id Betan, R. J. Liotta, N. Sandulescu, and T. Vertse, *Phys. Rev. Lett.* **89**, 042501 (2002).
- [27] R. Id Betan, R. J. Liotta, N. Sandulescu, and T. Vertse, *Phys. Rev. C* **67**, 014322 (2003).
- [28] G. Gamow, *Z. Phys.* **51**, 204 (1928); **52**, 510 (1928).
- [29] A. F. J. Siegert, *Phys. Rev.* **56**, 750 (1939).
- [30] T. Berggren, *Phys. Lett. B* **373**, 1 (1996).
- [31] Y. B. Zel'dovich, *Zh. Éksp. Teor. Fiz.* **39**, 776 (1960) [*Sov. Phys. JETP* **12**, 542 (1960)].
- [32] N. Hokkyo, *Prog. Theor. Phys.* **33**, 1116 (1965).
- [33] W. J. Romo, *Nucl. Phys.* **A116**, 617 (1968).
- [34] T. Berggren, *Nucl. Phys.* **A109**, 265 (1968).
- [35] B. Gyarmati and T. Vertse, *Nucl. Phys.* **A160**, 523 (1971).
- [36] G. Garcia-Calderon and R. Peierls, *Nucl. Phys.* **A265**, 443 (1976).
- [37] V. I. Kukulín, V. M. Krasnopol'sky, and J. Horáček, *Theory of Resonances* (Kluwer, Dordrecht, 1989).
- [38] P. Lind, *Phys. Rev. C* **47**, 1903 (1993).
- [39] R. G. Newton, *Scattering Theory of Waves and Particles* (Springer-Verlag, New York, 1982).
- [40] R. Jost, *Helv. Phys. Acta* **20**, 256 (1947).
- [41] T. Vertse, P. Curutchet, and R. J. Liotta, *Proceedings of the Symposium on Resonances*, edited by E. Brändas and N. Elander, *Lecture Notes in Physics*, Vol. 325 (Springer-Verlag, Berlin, 1987), p. 179.
- [42] R. J. Liotta, E. Maglione, N. Sandulescu, and T. Vertse, *Phys. Lett. B* **367**, 1 (1996).
- [43] T. Vertse, R. J. Liotta, W. Nazarewicz, N. Sandulescu, and A. T. Kruppa, *Phys. Rev. C* **57**, 3089 (1998).
- [44] G. G. Dussel, R. J. Liotta, H. Sofia, and T. Vertse, *Phys. Rev. C* **46**, 558 (1992).
- [45] S. Fortunato, A. Insolia, R. J. Liotta, and T. Vertse, *Phys. Rev. C* **54**, 3279 (1997).
- [46] O. Civitarese, R. J. Liotta, and T. Vertse, *Phys. Rev. C* **64**, 057305 (2001).
- [47] T. Vertse, R. J. Liotta, and E. Maglione, *Nucl. Phys.* **A584**, 13 (1995).
- [48] P. Lind, R. J. Liotta, E. Maglione, and T. Vertse, *Z. Phys. A* **347**, 231 (1994).
- [49] J. N. Ginocchio, *Ann. Phys. (N.Y.)* **152**, 203 (1984); **159**, 467 (1985).
- [50] I. M. Green and S. A. Moszkowski, *Phys. Rev.* **139**, B790 (1965).
- [51] R. B. Firestone and V. S. Shirley, *Table of Isotopes*, 8th ed. (Wiley, New York, 1996), Vol. 1.
- [52] B. Gyarmati, F. Krisztinkovics, and T. Vertse, *Phys. Lett.* **41B**, 475 (1972).
- [53] C. G. Bollini, O. Civitarese, A. L. De Paoli, and M. C. Rocca, *Phys. Lett. B* **382**, 205 (1996).
- [54] O. Civitarese, M. Gadella, and R. I. Betan, *Nucl. Phys.* **A660**, 255 (1999).